

Article

Stress-Controlled Frequency Tuning and Parametric Amplification of the Vibrations of Coupled Nanomembranes

Sepideh Naserbakht, Andreas Naesby and Aurélien Dantan * Department of Physics and Astronomy, University of Aarhus, DK-8000 Aarhus C, Denmark;
sepideh@phys.au.dk (S.N.); anr@mac.com (A.N.)

* Correspondence: dantan@phys.au.dk

Received: 24 October 2019; Accepted: 11 November 2019; Published: 12 November 2019



Abstract: Noninvasive tuning of the mechanical resonance frequencies of suspended parallel nanomembranes in various monolithic arrays is achieved by piezoelectric control of their tensile stress. Parametric amplification of their thermal fluctuations is shown to be enhanced by the piezoelectric actuation and amplification factors of up to 20 dB in the sub-parametric oscillation threshold regime are observed.

Keywords: nanomembrane resonators; stress engineering; parametric excitation; piezoelectrical actuation

1. Introduction

Suspended nano- and micro-resonators are ubiquitous in a wide range of sensing, photonics and telecommunication applications, for many of which a certain degree of tunability of their mechanical properties may be desirable [1,2]. Dynamical tuning of the mechanics can be achieved by modifying the stress of the resonant structures, e.g., capacitively [1,3], electro- [4–6] or photo-thermally [7–9], by bending [10] or by heating [11]. In general, such a stress control may allow for modifying not only the mechanical resonance frequencies and quality factors, but also the nonlinear response of the resonators [1,12–14]. Such a tunability is particularly interesting for *arrays* consisting of multiple resonators, for instance to match or enhance their collective response and sensing capabilities [15–17], to engineer and investigate complex collective dynamics [18–22], or to coherently manipulate phonons between them [23–31].

Suspended drum-shaped resonators, made of low loss material such as silicon nitride and possessing high mechanical quality factors, can be efficiently coupled to electromagnetic fields, whether in the optical or microwave/radiofrequency domains [32–39]. Having multiple such membrane resonators [40–43] simultaneously interacting with cavity fields opens up opportunities for a number of exciting applications, e.g., collectively enhanced optomechanics [44–47], optomechanical synchronization [48], phonon transport [49,50] or entanglement and multimode squeezing generation [51–55].

We investigate here the tuning of the linear and nonlinear mechanical properties of suspended silicon nitride square drums by the application of a piezoelectrically controlled force to the chip supporting the drums. In this scheme, recently implemented with a single [56] and pairs of membranes [43,57], the compression of the frame caused by the piezoelectric force modifies the tensile stress of the silicon nitride films, thereby allowing for reversibly tuning the mechanical resonance frequencies without deteriorating their quality factors. We report here on the simultaneous tuning of the mechanical resonance frequencies of the membranes of various monolithic double-membrane arrays, and show for instance that the modes of membranes with close resonance frequencies can be tuned to degeneracy by the application of a bias voltage to the piezoelectric element. This tunability

would be essential in the abovementioned applications involving optomechanical arrays. In addition to radiation pressure, such drum resonators naturally lend themselves to fluid pressure measurements, and the tuning of their mechanical properties within such compact monolithic arrays would also be highly interesting in connection with the realization of squeeze film pressure sensors [58,59].

Furthermore, as we recently reported in [57], such a piezoelectric stress control allows for enhancing the resonators' nonlinear response to dynamical actuation. We expand here on this demonstration by performing detailed studies of the parametric excitation of the thermal fluctuations of the fundamental drummodes of two closely lying membranes in a monolithic array, for which amplification factors of up to 20 dB in the sub-parametric oscillation threshold regime are observed. The observed noise spectra and gains are in excellent agreement with the predictions of a simple phase-averaged subthreshold parametric amplification model.

Mechanical parametric amplification [60] being an ubiquitous tool in electro-opto-mechanical systems [61] to investigate and exploit nonlinear dynamics in a wide range of MEMS applications and resonators [1,13,14,17,26,62–68], the results demonstrated here with suspended silicon nitride drum resonators open up opportunities for interesting applications involving thermomechanical squeezing [27,54–56,69–71] and amplification [68,72,73] in cavity electro/optomechanics, among others.

2. Electromechanical Resonators and Experimental Setup

The membrane resonators used in this work are commercial [74], high tensile stress (0.7–0.9 GPa), stoichiometric SiN square drums with lateral dimension 500 μm and thickness 100 nm, deposited on a Si frame with lateral dimension 5 mm and thickness of either 200 or 500 μm . As described in [57] and depicted in Figure 1a,b, three corners of a Si chip were glued by application and curing of a small dab of UV-resist (OrmoComp, Micro resist technology GmbH) onto a piezoelectric ring actuator with 6 mm inner diameter (Noliac NAC2123) to which both dc and ac voltages can be applied. Following the method of [40], double-membrane arrays were made by gluing the two chips together either on top of each other (Figure 1c), so that the intermembrane separation was given by the Si frame thickness (200 μm in this case), or with a spacer in between the SiN films setting the separation between the suspended membranes to be $\sim 8.5 \mu\text{m}$ (Figure 1d).

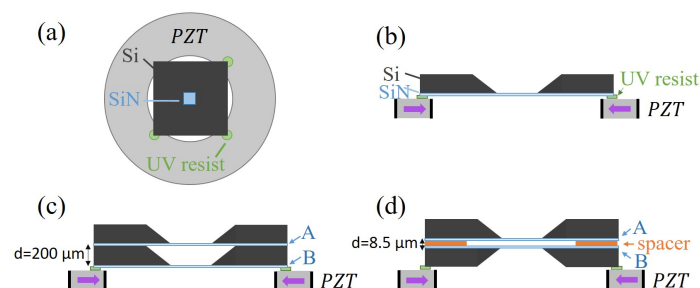


Figure 1. (a) Top view schematic of the membrane chip mounted on a piezoelectric ring actuator. (b–d) Sideview schematics of the single- or double-membrane electromechanical resonators studied. The purple arrows inside the piezoelectric transducer (PZT) indicate the direction of the compressive force for a positive voltage difference between the outer and inner electrodes.

The vibrations of the membranes can then be measured by monitoring the transmission of monochromatic light ($\sim 900 \text{ nm}$) issued from an external cavity diode laser through a linear Fabry–Perot interferometer constituted by the membrane—or membrane array—and a 50:50 beamsplitter mirror positioned parallel to the membranes at a distance of approximately 7 mm (Figure 2). The fluctuations of the transmitted light are detected with a fast photodiode and analyzed with a narrow resolution bandwidth spectrum analyzer. The wavelength of the light is chosen so as to maximize the sensitivity of the interferometer to the displacement of the membrane modes

considered [40]. The mechanical resonance frequencies can be determined by Lorentzian fits to the thermal noise spectrum, typically recorded with a resolution bandwidth (RBW) of 0.5 Hz and averaged 500 times. The mechanical quality factors are determined either from the results of the Lorentzian fits to the thermal noise spectrum, or by performing ringdown spectroscopy of the resonantly excited mode [40,58].

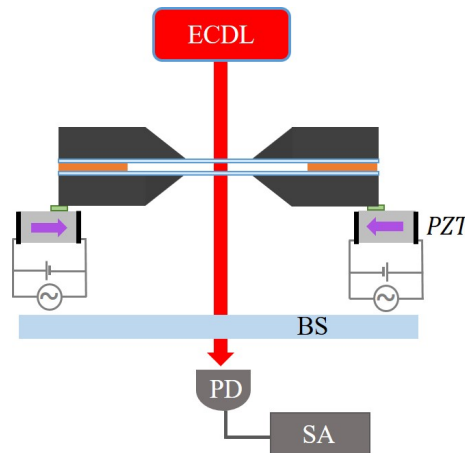


Figure 2. Schematic experimental setup for the piezoelectric actuation and detection of the membrane vibrations (shown here for the array geometry of Figure 1d). ECDL: external cavity diode laser, BS: beamsplitter mirror, PZT: piezoelectric transducer, PD: photodiode, SA: spectrum analyzer.

3. Mechanical Frequency Tuning

The application of a positive voltage to a single membrane chip with a 200 μm -thick frame, as depicted in Figure 1b, results in a reduction of the tensile stress of the SiN film. In this tensile stress-dominated regime the resonance (angular) frequencies of the mechanical modes are to a very good approximation given by

$$\omega_{m,n} = \sqrt{\frac{\mathcal{T}}{\rho}} \frac{\pi}{a} \sqrt{m^2 + n^2}, \quad (1)$$

where \mathcal{T} is the tensile stress, ρ the density of SiN, a the membrane lateral dimension and m, n strictly positive integers, and can thus be tuned by the application of a bias voltage V_{dc} to the piezoelectric element, as demonstrated in [56]. A linear reduction with V_{dc} of the resonance frequencies of both the fundamental ($m = 1, n = 1$) and a higher order ($m = 3, n = 3$) modes is observed (Figure 3a,b), with frequency shifts of -43 Hz/V and -130 Hz/V , respectively. Furthermore, as shown in Figure 3c, the mechanical quality factors are observed to be only weakly (slight increase for this sample) dependent on the bias voltage.

We now turn to the piezoelectric actuation of double-membrane arrays as depicted in Figure 1c,d. The compression of the piezoelectric transducer (PZT) affects the whole Si frame/SiN films structure. In both geometries the lower (closer to the piezoelectric element) membrane sees its tensile stress decrease when a positive dc-voltage is applied to the PZT, whereas the upper (further away from the piezoelectric element) sees its stress increase. Figure 3d,e shows the variations with the bias voltage of the (1,1) and (3,3) modes of an array with a 200 μm -thick frame. Shifts of -16 Hz/V and -44 Hz/V are respectively observed for the (1,1) and (3,3) modes of the lower membrane, and 9 Hz/V and 29 Hz/V for those of the upper membrane. The mechanical quality factors are observed to be essentially independent of the bias voltage (Figure 3f).

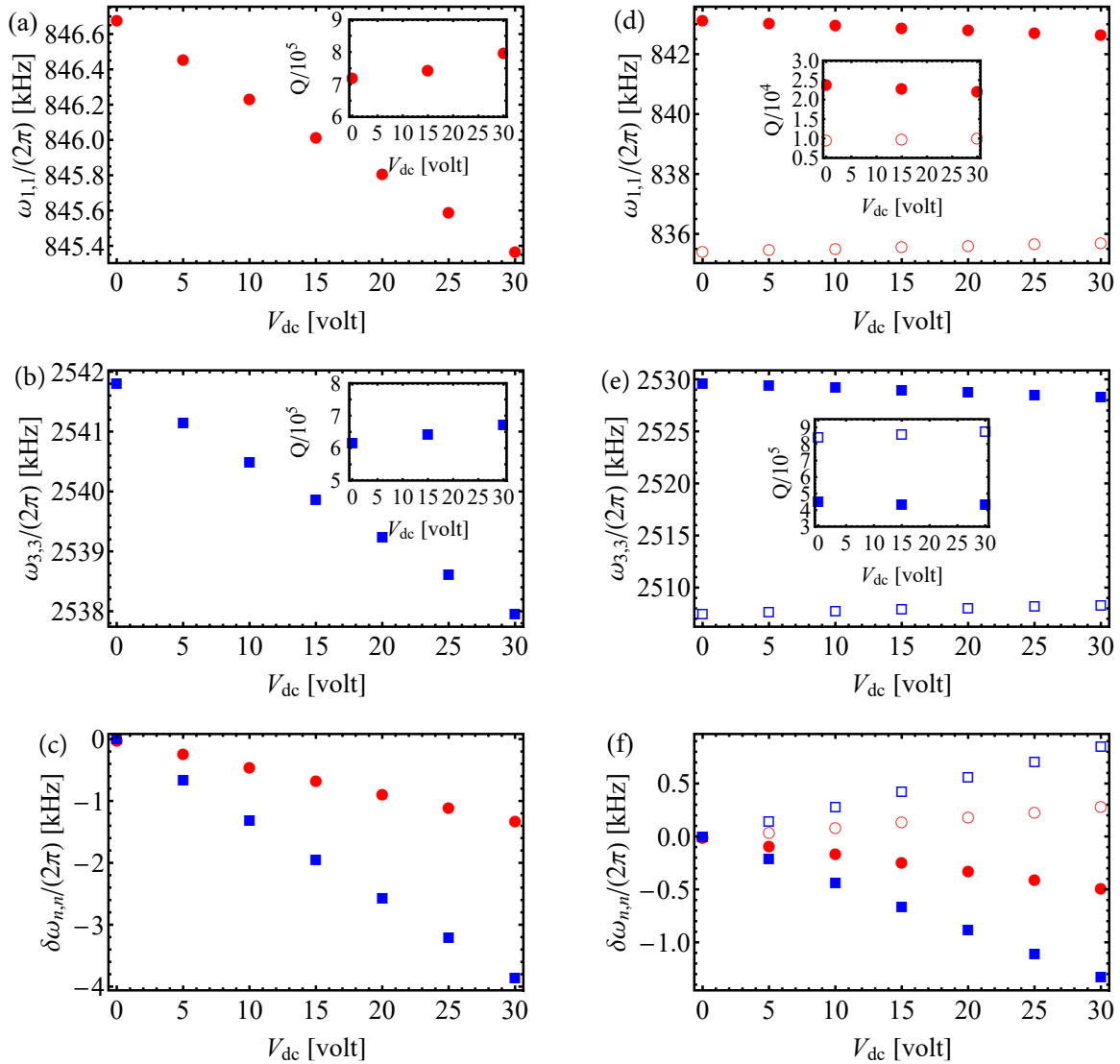


Figure 3. (a,b) Measured *single membrane* (1,1) and (3,3) mode frequencies as a function of bias voltage V_{dc} . (c) Corresponding resonance frequencies shifts versus V_{dc} . (d,e) Measured (1,1) and (3,3) mode resonance frequencies of the A (red circles and empty blue squares) and B (red dots and filled blue squares) membranes in a *double-membrane* array as in Figure 1c, as a function of V_{dc} . (f) Corresponding resonance frequency shifts versus V_{dc} . The error bars are smaller than the size of the data points. The insets in (a,b) and (d,e) show the variations of the mechanical quality factors with V_{dc} .

Piezoelectric tuning of the modes of a shorter ($\sim 8.5 \mu\text{m}$) array with thicker frame ($500 \mu\text{m}$) and in the geometry of Figure 1d was also demonstrated and reported in [57]. Figure 4a,b shows the variations with V_{dc} of the resonance frequencies of the (1,1) and (2,2) modes of both membranes. The two membranes of this array exhibit fairly similar bare mechanical properties; for instance, the fundamental modes of the upper (A) and lower (B) membranes have resonance frequencies 721.05 kHz and 721.55 kHz, respectively, in absence of biasing. It is then possible to tune them to degeneracy by applying a bias voltage of approximately 56 V, as shown in Figure 4. The mechanical quality factors are also observed to be essentially independent of the bias voltage for this sample [57]. A careful analysis of the evolution of the thermal noise spectra allows furthermore for extracting the intermembrane coupling, as discussed in [57].

Having demonstrated the possibility to noninvasively tune the mechanical mode spectrum of such vertically coupled membrane systems, we now turn to their dynamical activation under parametric excitation.

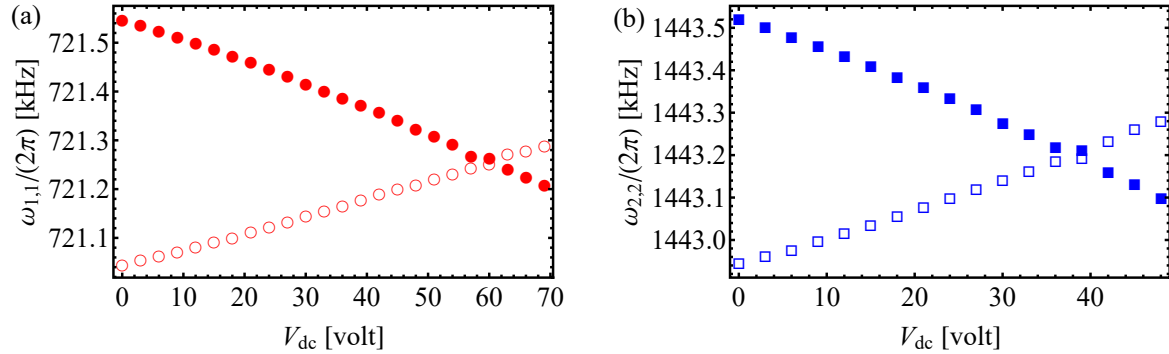


Figure 4. (a) Measured (1,1) mode resonance frequencies of the A (red circles) and B (red dots) membranes in a double-membrane array as in Figure 1d, as a function of V_{dc} . (b) Measured (2,2) mode resonance frequencies of the A (empty blue squares) and B (filled blue squares) membranes, as a function of V_{dc} .

4. Parametric Amplification of the Thermal Fluctuations

4.1. Theoretical Model

We consider a parametric modulation of the spring constant of a normal mode of the form $k = k_0[1 + \zeta \sin(\omega_p t)]$, where k_0 is the spring constant in absence of modulation, ζ the normalized modulation amplitude, which is proportional to the applied modulation voltage amplitude and ω_p the pump modulation frequency. The classical dynamics of the amplitude around equilibrium, $x(t)$, can be modeled by the following differential equation [60]

$$\ddot{x} + \Gamma \dot{x} + \omega_m^2 [1 + \zeta \sin(\omega_p t)] x = F_{th} / m, \tag{2}$$

where $\omega_m = \sqrt{k_0/m}$ is the bare mechanical resonance frequency of the normal mode considered, m the effective mass of the mode, $\Gamma = \omega_m/Q$ its damping rate and F_{th} a thermal noise force arising from the coupling with the thermal environment. For a high quality factor oscillator ($\omega_m \gg \Gamma$) and a pump modulation frequency $\omega_p = 2(\omega_m + \delta)$ close to the second harmonic frequency, it is convenient to introduce the slowly varying envelope $A(t)$ defined by

$$x(t) = [A(t)e^{-i\omega_m t} + A^*(t)e^{i\omega_m t}] / 2 \tag{3}$$

$$= X_1(t) \cos(\omega_m t) + X_2(t) \sin(\omega_m t) \tag{4}$$

where the quadratures X_1 and X_2 are respectively given by the real and imaginary parts of A . Under the rotating wave approximation, Equation (2) yields

$$\dot{A} = -\left(\frac{\Gamma}{2} + i\delta\right) A + \omega_m \frac{\zeta}{4} A^* + \tilde{F}, \tag{5}$$

where $\tilde{F} = F_{th}e^{i\omega_m t} / m\omega_m$. Fourier transforming Equation (5) using the convention $f(\omega) = \int f(t)e^{-i\omega t} dt$ yields

$$(\gamma + i\omega + i\delta) A(\omega) - \gamma \epsilon A^*(\omega) = \tilde{F}(\omega), \tag{6}$$

where

$$\gamma = \frac{\Gamma}{2} \quad \text{and} \quad \epsilon = \frac{\omega_m \zeta}{4\gamma} = \frac{Q\zeta}{2}. \tag{7}$$

From Equation (6) and its complex conjugate one readily obtains

$$A(\omega) = \frac{(\gamma + i\omega - i\delta)\tilde{F}(\omega) + \gamma\epsilon\tilde{F}^*(\omega)}{(\gamma + i\omega + i\delta)(\gamma + i\omega - i\delta) - (\gamma\epsilon)^2}, \tag{8}$$

$$A^*(\omega) = \frac{(\gamma + i\omega + i\delta)\tilde{F}^*(\omega) + \gamma\epsilon\tilde{F}(\omega)}{(\gamma + i\omega + i\delta)(\gamma + i\omega - i\delta) - (\gamma\epsilon)^2}. \tag{9}$$

The noise spectrum, $S_{X_\theta}(\omega) = \langle X_\theta(\omega)X_\theta(-\omega) \rangle$, of an arbitrary quadrature $X_\theta = X_1 \cos(\theta) + X_2 \sin(\theta)$ can be computed using the fact that

$$\langle F_{th}(\omega)F_{th}(\omega') \rangle = 4k_B T m \Gamma \delta(\omega + \omega'), \tag{10}$$

such that only $\langle \tilde{F}(\omega)\tilde{F}^*(-\omega) \rangle$ and $\langle \tilde{F}^*(\omega)\tilde{F}(-\omega) \rangle$ are nonzero and both equal to $4k_B T \gamma / m \omega_m^2$, where k_B is the Boltzmann constant and T the thermal bath temperature.

If, like in the experiment, one does not keep track of the quadrature angle θ , one observes an average noise spectrum

$$\bar{S}(\omega) \equiv \bar{S}_{X_\theta}(\omega) = \langle A(\omega)A^*(-\omega) + A^*(\omega)A(-\omega) \rangle / 4 \tag{11}$$

given by

$$\bar{S}(\omega) = \frac{4k_B T \gamma}{m \omega_m^2} \frac{\gamma^2(1 + \epsilon^2) + \omega^2 + \delta^2}{[\gamma^2(1 - \epsilon^2) + \delta^2 - \omega^2]^2 + 4\gamma^2 \omega^2}. \tag{12}$$

At the parametric resonance ($\delta = 0$), the average noise spectrum in Equation (12) can be simply written as

$$\bar{S}_{\delta=0}(\omega) = \frac{2k_B T \gamma}{m \omega_m^2} \left[\frac{1}{\gamma^2(1 - \epsilon)^2 + \omega^2} + \frac{1}{\gamma^2(1 + \epsilon)^2 + \omega^2} \right] \tag{13}$$

i.e., the sum of two Lorentzians with HWHMs (half-width at half-maximum) $\gamma(1 - \epsilon)$ and $\gamma(1 + \epsilon)$, corresponding to the noise spectrum of the amplified and deamplified quadratures, respectively. While in general not Lorentzian, the average noise spectrum is, to a good approximation, Lorentzian either at low gains ($\epsilon \ll 1$) or close to the parametric threshold $\epsilon \rightarrow 1$, where the contribution of the amplified quadrature noise dominates. At the parametric threshold $\epsilon = 1$ —or, equivalently, $\zeta = 2/Q$ —the linewidth of the noise spectrum diverges (in absence of nonlinearities).

The variance of the amplitude, $\Delta x^2 = \langle x^2 \rangle$, is obtained by integrating this one-sided noise spectrum over the positive frequencies

$$\Delta x^2 = \int_0^\infty \bar{S}(\omega) \frac{d\omega}{2\pi} \tag{14}$$

to give the average energy in the mode $\bar{E} = \frac{1}{2} m \omega_m^2 \langle x^2 \rangle$ as

$$\bar{E} = \frac{\bar{E}_0}{1 - \epsilon^2 / (1 + \delta^2 / \gamma^2)}, \tag{15}$$

where $\bar{E}_0 = \frac{1}{2} k_B T$ is the average energy in absence of parametric modulation. In presence of parametric modulation the average energy thus increases with the modulation amplitude as $1/(1 - \epsilon^2)$ and diverges at the threshold. For a nonzero pump detuning, the amplification is reduced with respect to that on resonance according to Equation (15) and the parametric resonance linewidth depends on both Γ and ϵ .

4.2. Experimental Results

Parametric excitation of the membranes of the 8.5 μm -long array, whose dc-actuation was shown in Figure 4, was investigated for different values of the biased voltage by applying a resonant parametric

modulation at the second harmonic frequency of the fundamental mode of one of the membranes. The evolution of the noise spectrum of the fundamental modes was then monitored as a function of the modulation voltage amplitude V_{ac} . The bias voltage V_{dc} , which determined the frequency separation between the fundamental mode frequencies $\Delta = \omega_{1,1}^B - \omega_{1,1}^A$ (difference between the filled and open circles in Figure 4a), was chosen in such a way that the second harmonic of the excited fundamental mode frequency, $2\omega_{1,1}^A$ or $2\omega_{1,1}^B$, did not coincide with a (2,2) mode resonance frequency. We verified experimentally that neither the non-resonantly driven (1,1) mode nor the (2,2) modes were excited in presence of the parametric drive.

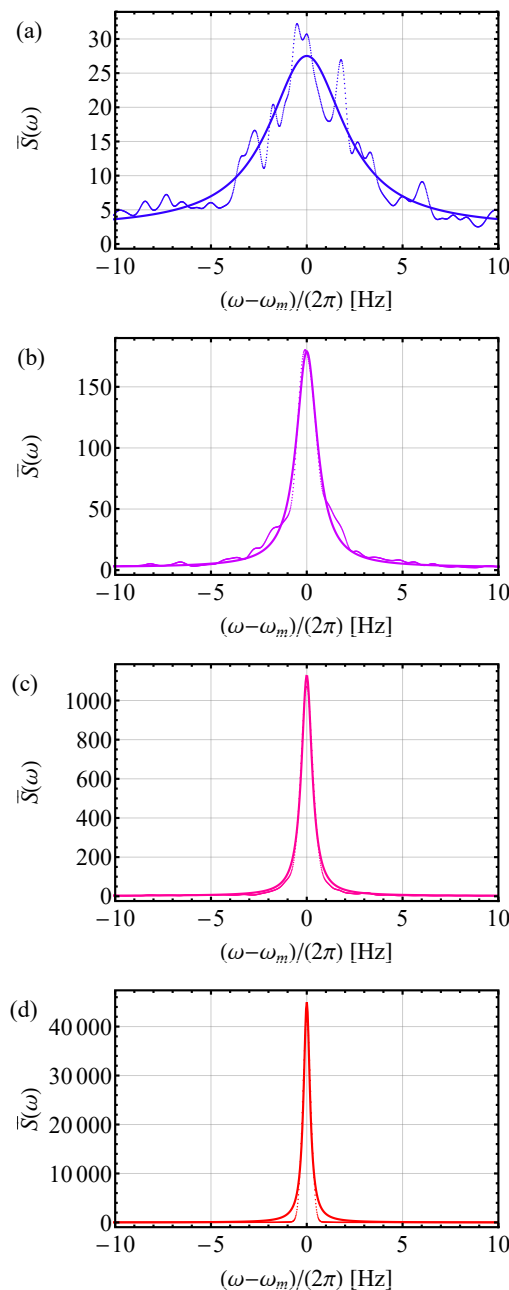


Figure 5. Average noise spectra of membrane B’s fundamental mode at a bias voltage corresponding to $\Delta/(2\pi) = 30$ Hz and for different resonant modulation amplitudes corresponding to (a) $\epsilon = 0.069$, (b) $\epsilon = 0.809$, (c) $\epsilon = 0.908$ and (d) $\epsilon = 0.996$. The solid lines are the results of Lorentzian fits to the data. The y-axis scale, in arbitrary units, is the same for all figures. The same RBW of 0.5 Hz is used for recording all the spectra.

Figure 5 shows examples of noise spectra of membrane B’s fundamental mode, obtained for a bias voltage corresponding to a frequency separation $\Delta/(2\pi) = 30$ Hz, and for increasing modulation amplitudes (see Supplementary Material for the complete spectrum dataset). The modulation amplitudes were normalized to the parametric threshold voltage and the same resolution bandwidth of 0.5 Hz is used for all spectra. The results of Lorentzian fits to the data are also shown. It can be seen that the amplified noise spectra are generally well-approximated by Lorentzians with increasing peak value/area and reduced linewidth, as the parametric modulation amplitude is increased.

The average energy is obtained by numerical integration of the spectrum and the energy gain—i.e., the ratio \bar{E}/\bar{E}_0 of the average energy for a given ϵ to the average energy for $\epsilon = 0$ —is shown in Figure 6a as a function of ϵ . The variations with ϵ of the HWHM obtained from the Lorentzian fits is also shown in Figure 6b. The solid line in Figure 6a shows the result of a fit according to Equation (15), while that in Figure 6b shows a linearly decreasing linewidth of the form $\gamma_B(1 - \epsilon)$, where γ_B is the HWHM in absence of modulation. As one approaches the threshold, effects due to the finite resolution bandwidth of the spectrum analyzer become visible and the measured linewidth is effectively limited by the RBW. Note that this does not affect the determination of the average energy, however, since the latter is related to the numerical integration of the noise spectrum and is independent of the RBW. Gains in energy of up to 125 (21 dB) were observed for this mode at this particular bias voltage, before the parametric oscillation threshold was reached. Similar behaviors were observed for both fundamental modes and different bias voltages (see Figure 8 and Supplementary Material), albeit with different gains and thresholds, as will be discussed below.

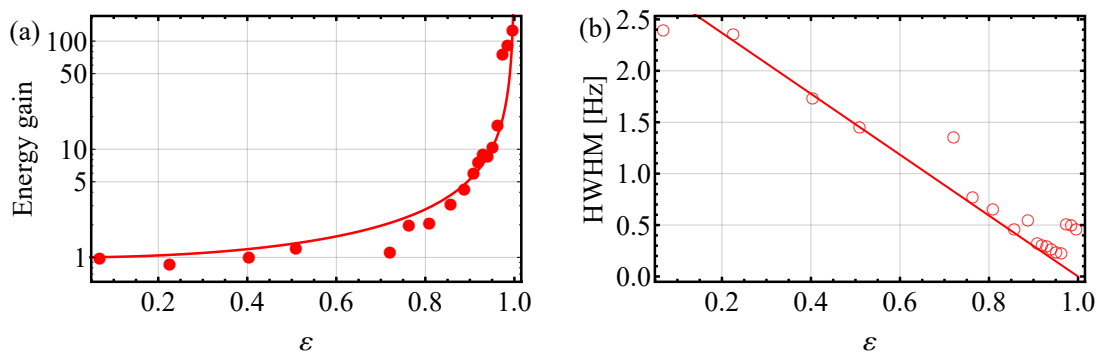


Figure 6. (a) Energy gain \bar{E}/\bar{E}_0 as a function of the normalized parametric modulation amplitude ϵ for membrane B’s fundamental mode at a bias voltage corresponding to $\Delta/(2\pi) = 30$ Hz. The solid line shows the result of a fit according to Equation (15). (b) HWHM of the noise spectra resulting from the Lorentzian fits, as a function of ϵ . The solid line shows a linearly decreasing function of the form $\gamma_B(1 - \epsilon)$.

The resonant nature of the parametric excitation was also verified by scanning the modulation voltage frequency around the second harmonic frequency. Figure 7 shows the variation of the energy gain—deduced from the noise spectra as previously—as a function of the pump detuning δ , for the fundamental mode of membrane B at a bias voltage such that $\Delta/(2\pi) = 250$ Hz and for two different parametric modulation amplitudes close to the threshold. The solid lines show the theoretical predictions of Equation (15), in which ϵ is determined by the zero-detuning value and γ is the HWHM measured in absence of modulation.

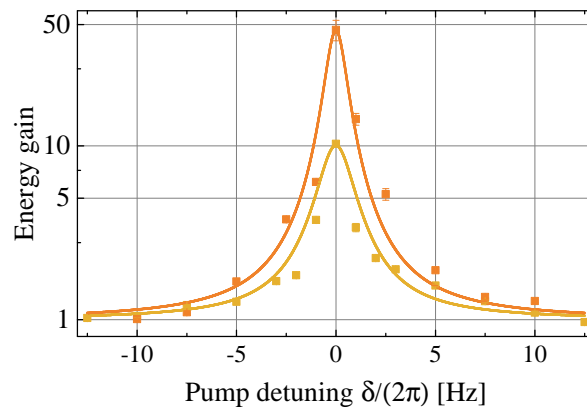


Figure 7. Energy gain as a function of pump detuning δ for the fundamental mode of membrane B for $\Delta/(2\pi) = 250$ Hz and for two modulation voltage amplitudes corresponding to $\epsilon = 0.949$ (yellow) and $\epsilon = 0.989$ (orange). The solid lines are the theoretical predictions of Equation (15).

We finally investigated the influence of the bias voltage V_{dc} on the resonant parametric amplification of the fundamental modes of both membranes. The energy gains of both modes for different bias voltages are shown in Figure 8 as a function of the resonant modulation amplitude. The amplitude was arbitrarily normalized to the parametric amplification threshold amplitude, $V_{ac} = 448$ mV, of membrane A's fundamental mode at $\Delta/(2\pi) = 250$ Hz. One first observes that increasing the bias voltage leads to lower parametric oscillation thresholds for both membranes. Higher thresholds for membrane A than for membrane B at comparable V_{dc} s were also systematically observed. The reasons for this behavior were investigated in detail in [57]. In brief, the lower membrane (B) experiences a direct modulation of its tensile stress at the parametric resonance frequency through the compression of the lower frame. The parametric oscillation threshold can be reached by the application of a moderate modulation voltage. In contrast, such a direct modulation of the SiN film spring constant is much weaker for the upper membrane (A). However, the application of a static compressive force to the chips results in a modification of the nonlinear response/stress of membrane A, which accounts for the lowering of the parametric amplification threshold with the bias voltage. Let us also note that, due to thermal drifts during the measurements, variations in the highest achievable gains close to the threshold were typically observed, so that one cannot rule out that higher subthreshold gain values may be achievable by better temperature control. Let us also remark that, at degeneracy ($\Delta = 0$), the single parametrically excited mode picture breaks down, as the dynamics of the two coupled modes have in principle to be taken into account [27]. However, since the parametric gain for membrane B is substantially stronger than for membrane A, the total amplified noise spectrum becomes quickly dominated by that of membrane B's fundamental mode, as the modulation amplitude increases. The observed parametric gains and threshold values thus consistently follow those of membrane B.

5. Conclusions

Noninvasive tuning of the mechanical resonance frequencies of suspended square drum resonators in monolithic vertical arrays was demonstrated using a simple scheme where the membrane chips were directly mounted on a piezoelectric ring actuator. The application of a piezoelectrically controlled force to the bottom chip allowed for modifying the tensile stress of the membrane resonators and thereby change their frequencies. For membranes with not too different bare mechanical frequencies, tuning to degeneracy by the application of a dc-voltage to the PZT is possible, as the bottom and top membrane experience opposite frequency shifts with the bias voltage.

Dynamical actuation of both membranes was also demonstrated by the application of an ac-voltage at twice the mechanical resonance frequencies of the fundamental modes of the membranes and observing the parametric amplification of their thermal fluctuations until the parametric oscillation threshold was reached. The experimental observations are well-accounted for by a simple

phase-averaged subthreshold parametric oscillator model. Last, the amplification was shown to be enhanced by the simultaneous application of the dc-voltage, which results in higher amplification gains and a lowering of the parametric oscillation thresholds.

Such a tuning of both the linear and nonlinear response of membrane resonators in vertical arrays is promising for exploring collective effects and investigating phonon dynamics in currently investigated optomechanical arrays [40–43], or for sensing applications [58,59,75].

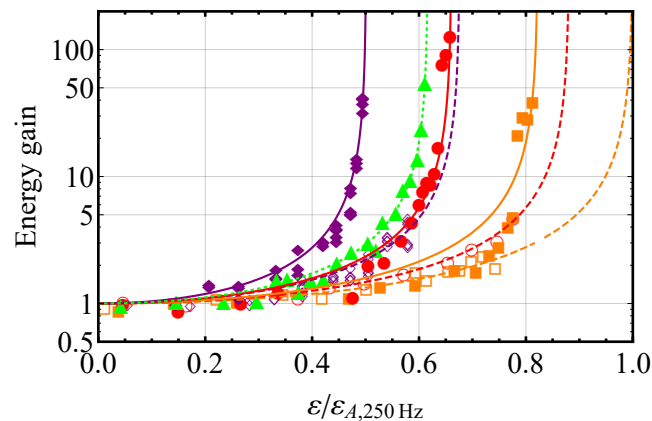


Figure 8. Energy gains as a function of normalized modulation amplitude for both fundamental modes for increasing V_{dc} , such that $\Delta/(2\pi) = 250$ Hz (yellow squares), 30 Hz (red circles) and -100 Hz (purple diamonds). The empty and full symbols are for membranes A and B, respectively. The green triangles correspond to the energy gain measured at the degeneracy ($\Delta = 0$). The modulation amplitude is arbitrarily normalized to the threshold amplitude for membrane A’s fundamental mode at $\Delta/(2\pi) = 250$ Hz. The solid lines show the results of fits to Equation (15).

Supplementary Materials: The following are available at www.mdpi.com/xxx/s1, Figure S1: Average noise spectra of membrane B’s fundamental mode for $\Delta/(2\pi) = 250$ Hz and different normalized modulation amplitude ϵ (top label of each subplot). The solid lines are the results of Lorentzian fits to the data. Figure S2: Average noise spectra of membrane B’s fundamental mode for $\Delta/(2\pi) = 30$ Hz and different normalized modulation amplitude ϵ (top label of each subplot). The solid lines are the results of Lorentzian fits to the data. Figure S3: Average noise spectra of membrane B’s fundamental mode for $\Delta/(2\pi) = -100$ Hz and different normalized modulation amplitude ϵ (top label of each subplot). The solid lines are the results of Lorentzian fits to the data. Figure S4: Average noise spectra of membrane A’s fundamental mode for $\Delta/(2\pi) = 250$ Hz and different normalized modulation amplitude ϵ (top label of each subplot). The solid lines are the results of Lorentzian fits to the data. Figure S5: Average noise spectra of membrane A’s fundamental mode for $\Delta/(2\pi) = 30$ Hz and different normalized modulation amplitude ϵ (top label of each subplot). The solid lines are the results of Lorentzian fits to the data. Figure S6: Average noise spectra of membrane A’s fundamental mode for $\Delta/(2\pi) = -100$ Hz and different normalized modulation amplitude ϵ (top label of each subplot). The solid lines are the results of Lorentzian fits to the data. Figure S7: Average noise spectra for $\Delta/(2\pi) = 0$ Hz and different normalized modulation amplitude ϵ (top label of each subplot). The solid lines are the results of Lorentzian fits to the data.

Author Contributions: conceptualization, A.D.; investigation, S.N. and A.N.; data curation, S.N. and A.N. and A.D.; writing—original draft preparation, A.D.; writing—review and editing, S.N. and A.N.; supervision, A.D.; funding acquisition, A.D.

Funding: This research was funded by the Velux Foundations.

Conflicts of Interest: The authors declare no conflict of interest.

References

1. Ekinci, K.L.; Roukes, M.L. Nanoelectromechanical systems. *Rev. Sci. Instrum.* **2005**, *76*, 061101. doi:10.1063/1.1927327. [CrossRef]
2. Li, M.; Tang, H.X.; Roukes, M.L. Ultra-sensitive NEMS-based cantilevers for sensing, scanned probe and very high-frequency applications. *Nat. Nanotechnol.* **2007**, *2*, 114. [CrossRef] [PubMed]
3. Kozinsky, I.; Postma, H.W.C.; Bargatin, I.; Roukes, M.L. Tuning nonlinearity, dynamic range, and frequency of nanomechanical resonators. *Appl. Phys. Lett.* **2006**, *88*, 253101. [CrossRef]

4. Jun, S.C.; Huang, X.M.H.; Manolidis, M.; Zorman, C.A.; Mehregany, M.; Hone, J. Electrothermal tuning of Al–SiC nanomechanical resonators. *Nanotechnology* **2006**, *17*, 1506–1511. doi:10.1088/0957-4484/17/5/057. [[CrossRef](#)]
5. Hüttel, A.K.; Steele, G.A.; Witkamp, B.; Poot, M.; Kouwenhoven, L.P.; van der Zant, H.S.J. Carbon Nanotubes as Ultrahigh Quality Factor Mechanical Resonators. *Nano Lett.* **2009**, *9*, 2547–2552. [[CrossRef](#)] [[PubMed](#)]
6. Barton, R.A.; Storch, I.R.; Adiga, V.P.; Sakakibara, R.; Cipriany, B.R.; Ilic, B.; Wang, S.P.; Ong, P.; McEuen, P.L.; Parpia, J.M.; et al. Photothermal Self-Oscillation and Laser Cooling of Graphene Optomechanical Systems. *Nano Lett.* **2012**, *12*, 4681–4686. [[CrossRef](#)] [[PubMed](#)]
7. Okamoto, H.; Kamada, T.; Onomitsu, K.; Mahboob, I.; Yamaguchi, H. Optical Tuning of Coupled Micromechanical Resonators. *Appl. Phys. Express* **2009**, *2*, 062202. doi:10.1143/apex.2.062202. [[CrossRef](#)]
8. Jöckel, A.; Rakher, M.T.; Korppi, M.; Camerer, S.; Hunger, D.; Mader, M.; Treutlein, P. Spectroscopy of mechanical dissipation in micro-mechanical membranes. *Appl. Phys. Lett.* **2011**, *99*, 143109. [[CrossRef](#)]
9. Inoue, T.; Anno, Y.; Imakita, Y.; Takei, K.; Arie, T.; Akita, S. Resonance Control of a Graphene Drum Resonator in a Nonlinear Regime by a Standing Wave of Light. *ACS Omega* **2017**, *2*, 5792–5797. doi:10.1021/acsomega.7b00699. [[CrossRef](#)] [[PubMed](#)]
10. Verbridge, S.S.; Shapiro, D.F.; Craighead, H.G.; Parpia, J.M. Macroscopic Tuning of Nanomechanics: Substrate Bending for Reversible Control of Frequency and Quality Factor of Nanostring Resonators. *Nano Lett.* **2007**, *7*, 1728–1735. [[CrossRef](#)] [[PubMed](#)]
11. St-Gelais, R.; Bernard, S.; Reinhardt, C.; Sankey, J.C. Swept-Frequency Drumhead Optomechanical Resonators. *ACS Photon.* **2019**, *6*, 525–530. doi:10.1021/acsp Photonics.8b01519. [[CrossRef](#)]
12. Almog, R.; Zaitsev, S.; Shtempluck, O.; Buks, E. Signal amplification in a nanomechanical Duffing resonator via stochastic resonance. *Appl. Phys. Lett.* **2007**, *90*, 013508. [[CrossRef](#)]
13. Antoni, T.; Makles, K.; Braive, R.; Briant, T.; Cohadon, P.F.; Sagnes, I.; Robert-Philip, I.; Heidmann, A. Nonlinear mechanics with suspended nanomembranes. *EPL (Europhys. Lett.)* **2012**, *100*, 68005. doi:10.1209/0295-5075/100/68005. [[CrossRef](#)]
14. Thomas, O.; Mathieu, F.; Mansfield, W.; Huang, C.; Trolrier-McKinstry, S.; Nicu, L. Efficient parametric amplification in micro-resonators with integrated piezoelectric actuation and sensing capabilities. *Appl. Phys. Lett.* **2013**, *102*, 163504. doi:10.1063/1.4802786. [[CrossRef](#)]
15. Buks, E.; Roukes, M.L. Electrically tunable collective response in a coupled micromechanical array. *J. Microelectromech. Syst.* **2002**, *11*, 802–807. doi:10.1109/JMEMS.2002.805056. [[CrossRef](#)]
16. Sage, E.; Sansa, M.; Fostner, S.; Defoort, M.; Gély, M.; Naik, A.K.; Morel, R.; Duraffourg, L.; Roukes, M.L.; Alava, T.; et al. Single-particle mass spectrometry with arrays of frequency-addressed nanomechanical resonators. *Nat. Commun.* **2018**, *9*, 3283. [[CrossRef](#)] [[PubMed](#)]
17. Zhao, C.; Zhou, X.; Pandit, M.; Sobreviela, G.; Du, S.; Zou, X.; Seshia, A. Toward High-Resolution Inertial Sensors Employing Parametric Modulation in Coupled Micromechanical Resonators. *Phys. Rev. Appl.* **2019**, *12*, 044005. doi:10.1103/PhysRevApplied.12.044005. [[CrossRef](#)]
18. Shim, S.B.; Imboden, M.; Mohanty, P. Synchronized Oscillation in Coupled Nanomechanical Oscillators. *Science* **2007**, *316*, 95–99. doi:10.1126/science.1137307. [[CrossRef](#)] [[PubMed](#)]
19. Matheny, M.H.; Grau, M.; Villanueva, L.G.; Karabalin, R.B.; Cross, M.C.; Roukes, M.L. Phase Synchronization of Two Anharmonic Nanomechanical Oscillators. *Phys. Rev. Lett.* **2014**, *112*, 014101. doi:10.1103/PhysRevLett.112.014101. [[CrossRef](#)] [[PubMed](#)]
20. Deng, G.W.; Zhu, D.; Wang, X.H.; Zou, C.L.; Wang, J.T.; Li, H.O.; Cao, G.; Liu, D.; Li, Y.; Xiao, M.; et al. Strongly Coupled Nanotube Electromechanical Resonators. *Nano Lett.* **2016**, *16*, 5456–5462. doi:10.1021/acs.nanolett.6b01875. [[CrossRef](#)] [[PubMed](#)]
21. Luo, G.; Zhang, Z.Z.; Deng, G.W.; Li, H.O.; Cao, G.; Xiao, M.; Guo, G.C.; Tian, L.; Guo, G.P. Strong indirect coupling between graphene-based mechanical resonators via a phonon cavity. *Nat. Commun.* **2018**, *9*, 383. [[CrossRef](#)] [[PubMed](#)]
22. Matheny, M.H.; Emenheiser, J.; Fon, W.; Chapman, A.; Salova, A.; Rohden, M.; Li, J.; Hudoba de Badyn, M.; Pósfai, M.; Duenas-Osorio, L.; et al. Exotic states in a simple network of nanoelectromechanical oscillators. *Science* **2019**, *363*. [[CrossRef](#)] [[PubMed](#)]
23. Bagheri, M.; Poot, M.; Li, M.; Pernice, W.P.H.; Tang, H.X. Dynamic manipulation of nanomechanical resonators in the high-amplitude regime and non-volatile mechanical memory operation. *Nat. Nanotechnol.* **2011**, *6*, 726–732. [[CrossRef](#)] [[PubMed](#)]

24. Mahboob, I.; Nishiguchi, K.; Okamoto, H.; Yamaguchi, H. Phonon-cavity electromechanics. *Nat. Phys.* **2012**, *8*, 503. [[CrossRef](#)]
25. Faust, T.; Rieger, J.; Seitner, M.J.; Kotthaus, J.P.; Weig, E.M. Coherent control of a classical nanomechanical two-level system. *Nat. Phys.* **2013**, *9*, 485. [[CrossRef](#)]
26. Okamoto, H.;ourgout, A.; Chang, C.Y.; Onomitsu, K.; Mahboob, I.; Chang, E.Y.; Yamaguchi, H. Coherent phonon manipulation in coupled mechanical resonators. *Nat. Phys.* **2013**, *9*, 480. [[CrossRef](#)]
27. Mahboob, I.; Okamoto, H.; Onomitsu, K.; Yamaguchi, H. Two-Mode Thermal-Noise Squeezing in an Electromechanical Resonator. *Phys. Rev. Lett.* **2014**, *113*, 167203. doi:10.1103/PhysRevLett.113.167203. [[CrossRef](#)] [[PubMed](#)]
28. Mathew, J.P.; Patel, R.N.; Borah, A.; Vijay, R.; Deshmukh, M.M. Dynamical strong coupling and parametric amplification of mechanical modes of graphene drums. *Nat. Nanotechnol.* **2016**, *11*, 747. [[CrossRef](#)] [[PubMed](#)]
29. Chen, C.; Zanette, D.H.; Czaplowski, D.A.; Shaw, S.; López, D. Direct observation of coherent energy transfer in nonlinear micromechanical oscillators. *Nat. Commun.* **2017**, *8*, 15523. [[CrossRef](#)] [[PubMed](#)]
30. Yang, F.; Rochau, F.; Huber, J.S.; Brioussel, A.; Rastelli, G.; Weig, E.M.; Scheer, E. Spatial Modulation of Nonlinear Flexural Vibrations of Membrane Resonators. *Phys. Rev. Lett.* **2019**, *122*, 154301. doi:10.1103/PhysRevLett.122.154301. [[CrossRef](#)] [[PubMed](#)]
31. Zhang, Z.Z.; Song, X.X.; Luo, G.; Su, Z.J.; Wang, K.L.; Cao, G.; Li, H.O.; Xiao, M.; Guo, G.C.; Tian, L.; et al. Coherent Phonon Dynamics in Spatially-Separated Graphene Mechanical Resonators. *arXiv* **2019**, arxiv:1909.11311. [[CrossRef](#)]
32. Thompson, J.D.; Zwickl, B.M.; Jayich, A.M.; Marquardt, F.; Girvin, S.M.; Harris, J.G.E. Strong dispersive coupling of a high-finesse cavity to a micromechanical membrane. *Nature* **2008**, *452*, 72–75. [[CrossRef](#)] [[PubMed](#)]
33. Wilson, D.J.; Regal, C.A.; Papp, S.B.; Kimble, H.J. Cavity Optomechanics with Stoichiometric SiN Films. *Phys. Rev. Lett.* **2009**, *103*, 207204. doi:10.1103/PhysRevLett.103.207204. [[CrossRef](#)] [[PubMed](#)]
34. Purdy, T.P.; Peterson, R.W.; Regal, C.A. Observation of Radiation Pressure Shot Noise on a Macroscopic Object. *Science* **2013**, *339*, 801–804. doi:10.1126/science.1231282. [[CrossRef](#)] [[PubMed](#)]
35. Bagci, T.; Simonsen, A.; Schmid, S.; Villanueva, L.G.; Zeuthen, E.; Appel, J.; Taylor, J.M.; Sørensen, A.; Usami, K.; Schliesser, A.; et al. Optical detection of radio waves through a nanomechanical transducer. *Nature* **2014**, *507*, 81. [[CrossRef](#)] [[PubMed](#)]
36. Andrews, R.W.; Peterson, R.W.; Purdy, T.P.; Cicak, K.; Simmonds, R.W.; Regal, C.A.; Lehnert, K.W. Bidirectional and efficient conversion between microwave and optical light. *Nat. Phys.* **2014**, *10*, 321. [[CrossRef](#)]
37. Yuan, M.; Singh, V.; Blanter, Y.M.; Steele, G.A. Large cooperativity and microkelvin cooling with a three-dimensional optomechanical cavity. *Nat. Commun.* **2015**, *6*, 8491. [[CrossRef](#)] [[PubMed](#)]
38. Xu, H.; Mason, D.; Jiang, L.; Harris, J.G.E. Topological energy transfer in an optomechanical system with exceptional points. *Nature* **2016**, *80*, 537. doi:10.1038/nature18604. [[CrossRef](#)] [[PubMed](#)]
39. Rossi, M.; Mason, D.; Chen, J.; Tsaturyan, Y.; Schliesser, A. Measurement-based quantum control of mechanical motion. *Nature* **2018**, *563*, 53–58. [[CrossRef](#)] [[PubMed](#)]
40. Nair, B.; Naesby, A.; Dantan, A. Optomechanical characterization of silicon nitride membrane arrays. *Opt. Lett.* **2017**, *42*, 1341–1344. doi:10.1364/OL.42.001341. [[CrossRef](#)] [[PubMed](#)]
41. Piergentili, P.; Catalini, L.; Bawaj, M.; Zippilli, S.; Malossi, N.; Natali, R.; Vitali, D.; Giuseppe, G.D. Two-membrane cavity optomechanics. *New J. Phys.* **2018**, *20*, 083024. [[CrossRef](#)]
42. Gärtner, C.; Moura, J.P.; Haaxman, W.; Norte, R.A.; Gröblacher, S. Integrated Optomechanical Arrays of Two High Reflectivity SiN Membranes. *Nano Lett.* **2018**, *18*, 7171–7175. [[CrossRef](#)] [[PubMed](#)]
43. Wei, X.; Sheng, J.; Yang, C.; Wu, Y.; Wu, H. Controllable two-membrane-in-the-middle cavity optomechanical system. *Phys. Rev. A* **2019**, *99*, 023851. doi:10.1103/PhysRevA.99.023851. [[CrossRef](#)]
44. Xuereb, A.; Genes, C.; Dantan, A. Strong Coupling and Long-Range Collective Interactions in Optomechanical Arrays. *Phys. Rev. Lett.* **2012**, *109*, 223601. doi:10.1103/PhysRevLett.109.223601. [[CrossRef](#)] [[PubMed](#)]
45. Xuereb, A.; Genes, C.; Dantan, A. Collectively enhanced optomechanical coupling in periodic arrays of scatterers. *Phys. Rev. A* **2013**, *88*, 053803. doi:10.1103/PhysRevA.88.053803. [[CrossRef](#)]
46. Seok, H.; Buchmann, L.F.; Singh, S.; Meystre, P. Optically mediated nonlinear quantum optomechanics. *Phys. Rev. A* **2012**, *86*, 063829. doi:10.1103/PhysRevA.86.063829. [[CrossRef](#)]

47. Kipf, T.; Agarwal, G.S. Superradiance and collective gain in multimode optomechanics. *Phys. Rev. A* **2014**, *90*, 053808. doi:10.1103/PhysRevA.90.053808. [[CrossRef](#)]
48. Bemani, F.; Motazedifard, A.; Roknizadeh, R.; Naderi, M.H.; Vitali, D. Synchronization dynamics of two nanomechanical membranes within a Fabry-Perot cavity. *Phys. Rev. A* **2017**, *96*, 023805. doi:10.1103/PhysRevA.96.023805. [[CrossRef](#)]
49. Xuereb, A.; Genes, C.; Pupillo, G.; Paternostro, M.; Dantan, A. Reconfigurable Long-Range Phonon Dynamics in Optomechanical Arrays. *Phys. Rev. Lett.* **2014**, *112*, 133604. doi:10.1103/PhysRevLett.112.133604. [[CrossRef](#)] [[PubMed](#)]
50. Xuereb, A.; Imperato, A.; Dantan, A. Heat transport in harmonic oscillator systems with thermal baths: application to optomechanical arrays. *New J. Phys.* **2015**, *17*, 055013. [[CrossRef](#)]
51. Bhattacharya, M.; Meystre, P. Multiple membrane cavity optomechanics. *Phys. Rev. A* **2008**, *78*, 041801. doi:10.1103/PhysRevA.78.041801. [[CrossRef](#)]
52. Hartmann, M.J.; Plenio, M.B. Steady State Entanglement in the Mechanical Vibrations of Two Dielectric Membranes. *Phys. Rev. Lett.* **2008**, *101*, 200503. doi:10.1103/PhysRevLett.101.200503. [[CrossRef](#)] [[PubMed](#)]
53. Nielsen, W.H.P.; Tsaturyan, Y.; Møller, C.B.; Polzik, E.S.; Schliesser, A. Multimode optomechanical system in the quantum regime. *Proc. Natl. Acad. Sci. USA* **2017**, *114*, 62. doi:10.1073/pnas.1608412114. [[CrossRef](#)] [[PubMed](#)]
54. Patil, Y.S.; Chakram, S.; Chang, L.; Vengalattore, M. Thermomechanical Two-Mode Squeezing in an Ultrahigh-Q Membrane Resonator. *Phys. Rev. Lett.* **2015**, *115*, 017202. doi:10.1103/PhysRevLett.115.017202. [[CrossRef](#)] [[PubMed](#)]
55. Pontin, A.; Bonaldi, M.; Borrielli, A.; Marconi, L.; Marino, F.; Pandraud, G.; Prodi, G.A.; Sarro, P.M.; Serra, E.; Marin, F. Dynamical Two-Mode Squeezing of Thermal Fluctuations in a Cavity Optomechanical System. *Phys. Rev. Lett.* **2016**, *116*, 103601. doi:10.1103/PhysRevLett.116.103601. [[CrossRef](#)] [[PubMed](#)]
56. Wu, S.; Sheng, J.; Zhang, X.; Wu, Y.; Wu, H. Parametric excitation of a SiN membrane via piezoelectricity. *AIP Adv.* **2018**, *8*, 015209. doi:10.1063/1.5009952. [[CrossRef](#)]
57. Naserbakht, S.; Naesby, A.; Dantan, A. Electromechanics in vertically coupled nanomembranes. *Appl. Phys. Lett.* **2019**, *115*, 061105. [[CrossRef](#)]
58. Naesby, A.; Naserbakht, S.; Dantan, A. Effects of pressure on suspended micromechanical membrane arrays. *Appl. Phys. Lett.* **2017**, *111*, 201103. doi:10.1063/1.5004261. [[CrossRef](#)]
59. Naserbakht, S.; Dantan, A. Squeeze film pressure sensors based on SiN membrane sandwiches. *Sens. Actuators A Phys.* **2019**, *298*, 111588. doi:10.1016/j.sna.2019.111588. [[CrossRef](#)]
60. Rugar, D.; Grütter, P. Mechanical parametric amplification and thermomechanical noise squeezing. *Phys. Rev. Lett.* **1991**, *67*, 699–702. doi:10.1103/PhysRevLett.67.699. [[CrossRef](#)] [[PubMed](#)]
61. Midolo, L.; Schliesser, A.; Fiore, A. Nano-opto-electro-mechanical systems. *Nat. Nanotechnol.* **2018**, *13*, 11–18. [[CrossRef](#)] [[PubMed](#)]
62. Turner, K.L.; Miller, S.A.; Hartwell, P.G.; MacDonald, N.C.; Strogatz, S.H.; Adams, S.G. Five parametric resonances in a microelectromechanical system. *Nature* **1998**, *396*, 149–152. [[CrossRef](#)]
63. Carr, D.W.; Evoy, S.; Sekaric, L.; Craighead, H.G.; Parpia, J.M. Parametric amplification in a torsional microresonator. *Appl. Phys. Lett.* **2000**, *77*, 1545–1547. doi:10.1063/1.1308270. [[CrossRef](#)]
64. Mahboob, I.; Yamaguchi, H. Piezoelectrically pumped parametric amplification and Q enhancement in an electromechanical oscillator. *Appl. Phys. Lett.* **2008**, *92*, 173109. doi:10.1063/1.2903709. [[CrossRef](#)]
65. Karabalin, R.B.; Masmanidis, S.C.; Roukes, M.L. Efficient parametric amplification in high and very high frequency piezoelectric nanoelectromechanical systems. *Appl. Phys. Lett.* **2010**, *97*, 183101. doi:10.1063/1.3505500. [[CrossRef](#)]
66. Seitner, M.J.; Abdi, M.; Ridolfo, A.; Hartmann, M.J.; Weig, E.M. Parametric Oscillation, Frequency Mixing, and Injection Locking of Strongly Coupled Nanomechanical Resonator Modes. *Phys. Rev. Lett.* **2017**, *118*, 254301. doi:10.1103/PhysRevLett.118.254301. [[CrossRef](#)] [[PubMed](#)]
67. Huber, J.S.; Rastelli, G.; Seitner, M.; Maximilian, J.; Köbl, J.; Belzig, W.; Dykman, M.I.; Weig, E.M. Squeezing of thermal fluctuations in a driven nanomechanical resonator. *arXiv* **2019**, arxiv:1903.07601. [[CrossRef](#)]
68. Bothner, D.; Yanai, S.; Iniguez-Rabago, A.; Yuan, M.; Blanter, Y.M.; Steele, G.A. Cavity electromechanics with parametric mechanical driving. *arXiv* **2019**, arxiv:1908.08496. [[CrossRef](#)]

69. Szorkovszky, A.; Doherty, A.C.; Harris, G.I.; Bowen, W.P. Mechanical Squeezing via Parametric Amplification and Weak Measurement. *Phys. Rev. Lett.* **2011**, *107*, 213603. doi:10.1103/PhysRevLett.107.213603. [[CrossRef](#)] [[PubMed](#)]
70. Farace, A.; Giovannetti, V. Enhancing quantum effects via periodic modulations in optomechanical systems. *Phys. Rev. A* **2012**, *86*, 013820. doi:10.1103/PhysRevA.86.013820. [[CrossRef](#)]
71. Szorkovszky, A.; Brawley, G.A.; Doherty, A.C.; Bowen, W.P. Strong Thermomechanical Squeezing via Weak Measurement. *Phys. Rev. Lett.* **2013**, *110*, 184301. doi:10.1103/PhysRevLett.110.184301. [[CrossRef](#)] [[PubMed](#)]
72. Lemonde, M.A.; Didier, N.; Clerk, A.A. Enhanced nonlinear interactions in quantum optomechanics via mechanical amplification. *Nat. Commun.* **2016**, *7*, 11338. [[CrossRef](#)] [[PubMed](#)]
73. Levitan, B.A.; Metelmann, A.; Clerk, A.A. Optomechanics with two-phonon driving. *New J. Phys.* **2016**, *18*, 093014. doi:10.1088/1367-2630/18/9/093014. [[CrossRef](#)]
74. Norcada Inc. Available online: www.norcada.com (accessed on 12 November 2019).
75. Naesby, A.; Dantan, A. Microcavities with suspended subwavelength structured mirrors. *Opt. Express* **2018**, *26*, 29886–29894. doi:10.1364/OE.26.029886. [[CrossRef](#)] [[PubMed](#)]



© 2019 by the authors. Licensee MDPI, Basel, Switzerland. This article is an open access article distributed under the terms and conditions of the Creative Commons Attribution (CC BY) license (<http://creativecommons.org/licenses/by/4.0/>).